Flow Control with Local Electromagnetic Braking in Continuous Casting of Steel Slabs

KEVIN CUKIERSKI and BRIAN G. THOMAS

A computational fluid flow model is applied to investigate the effects of varying submerged entry nozzle (SEN) submergence depth and electromagnetic brake (EMBr) field strength on flow in the mold cavity. The three-dimensional, steady K-ε model of the nozzle and liquid cavity in the mold used the magnetic induction method in FLUENT to incorporate the localized-type static EMBr field measured at a steel plant. The model was validated by comparing results with an analytical solution and with nail board and oscillation mark measurements collected at the plant. Increasing EMBr strength at a constant SEN depth is found to cause a deeper jet impingement, weaker upper recirculation zone and meniscus velocity, and a smaller meniscus wave. Increasing SEN depth without EMBr caused the same trends. Increasing SEN depth at a constant EMBr strength brought about the opposite: higher meniscus velocity, larger meniscus wave, and deeper penetration depth. Using the knowledge gained from this model, electromagnetic forces can be controlled to stabilize the fluid flow in the mold cavity and thereby minimize casting defects.

DOI: 10.1007/s11663-007-9109-3

I. INTRODUCTION

CONTINUOUS casting is used to solidify over 90 pct of the 1.1 billion tonnes of steel produced in the world each year.[1,2] Most of the defects affecting steel quality in this process are associated with fluid flow in the mold, so small improvements in flow pattern can have a big impact. Excessive surface velocity can entrain mold-slag inclusions and cause surface level variations and fluctuations with time that produce surface defects.[3] Insufficient surface flow allows meniscus freezing and related surface defects. Deep penetration of the jet entering the mold cavity encourages the capture of subsurface inclusions. Thus, the mold flow pattern must be carefully optimized to find windows of stable casting conditions which avoid these problems.

Fluid flow in the mold is controlled by many design and operation conditions. These include the submerged entry nozzle (SEN) and port design shape, the SEN submergence depth (distance from top of nozzle ports to mold top surface), mold size, casting speed, position of the flow-control mechanism (slide gate or stopper rod), the rate of inert gas injection, and the application of electromagnetic forces. Each of these factors must be adjusted with regard to the other factors in order to produce a good flow pattern.[3] Although electromagnetics have great potential by improving the ability to control fluid flow in the mold cavity, their application is only effective as part of a complete flow-system design. Furthermore, flow in the steel caster is difficult to measure and computational models offer one of the few ways to understand the effect of electromagnetic forces on flow.

This article applies validated computational models to improve understanding of how to apply electromagnetics to improve fluid flow in the mold cavity. Electromagnetics can produce stirring, accelerating, or braking of flow and can be divided into two categories: electromagnetic stirrers (EMS) and electromagnetic brakes (EMBr).

Electromagnetic stirrers employ alternating current to generate a continuously-varying magnetic field to control flow in the mold cavity. Slab-mold EMS employs two stirrers on each wide side of the mold near the meniscus. These magnetic systems sequence the forces to circulate the flow around the mold perimeter, which homogenizes meniscus temperature, thus improving the quality of the finished slab.[5,6] Okazawa *et al.* used an large eddy simulation (LES) model and an experimental mercury model to study the effect of EMS magnet placement on flow circulation. The predicted velocities matched the measurements in the mercury model obtained with a Vives-type sensor.[4]

Multimode EMS (MM-EMS) uses two stirrers on each wide side located near the SEN port outlets.[5] This complex EMS system has three modes of operation. The electromagnetic level stabilizer (EMLS) mode directs the forces to oppose flow exiting the SEN, reduce surface velocity, and flatten the meniscus profile. Ishii *et al.* used a Reynolds-averaged Navier–Stokes (RANS) model to simulate the EMLS mode[7] and found that EMLS can effectively suppress meniscus velocity, especially for thin-slab casters. The electromagnetic level accelerator (EMLA) mode accelerates flow exiting the SEN, to increase both surface velocity and heat transfer to the meniscus. Kubota *et al.* reports that using both EMLS

KEVIN CUKIERSKI, Master's Candidate, and BRIAN G. THOMAS, Wilkins Professor of Mechanical Engineering, are with the Department of Mechanical and Industrial Engineering, University of Illinois at Urbana–Champaign, Urbana, IL. Contact e-mail: bgthomas@uiuc.edu

Manuscript submitted September 13, 2007.
Article published online December 8, 2007.

and EMLA together can effectively control meniscus velocity and reduce mold-slag entrapment, depending on casting conditions.[8] Finally, the electromagnetic rotary stirrer (EMRS) mode sequences the flow-to-stir and encourages mixing. Dauby *et al.* showed that if used optimally, MM-EMS can effectively maintain a favorable double-roll flow pattern in the mold cavity and reduce breakouts as well as the number of inclusions, cracks, and slivers present in the final product.[9]

Electromagnetic brakes employ coils with direct current to generate a static magnetic field to affect flow in the mold cavity. Like EMS, there are multiple types of EMBr that have various uses. Local EMBr uses two magnets on each wide side that aim to create rectangular regions of magnetic field near the SEN ports. This system is used to slow and diffuse the jet exiting the nozzle in order to decrease meniscus velocity and fluctuations in the meniscus profile.[10] Ha *et al.* used a RANS model to perform a three-dimensional simulation of flow in the mold cavity with EMBr, including heat transfer and shell solidification.[11] It was found that the addition of EMBr effectively slows flow exiting the nozzle, reduces impingement impact of the jet on the narrow face, and shortens the penetration depth of the lower recirculation zone. Takatani *et al.* used a similar method and found that the addition of EMBr causes an overall decrease of fluid velocities in the mold cavity, and that imposing a strong magnetic field can cause the jet to bend and dissipate before impinging against the narrow face.[12] Kim *et al.* showed that the addition of a local EMBr caused a vast decrease in jet momentum and velocity.[13]

Ruler EMBr uses two thin rectangular magnets located below the SEN ports on opposite sides of the mold, each of which spans across the entire wide side. Like the local EMBr, this is used to stabilize the meniscus velocity and meniscus profile.[12] Harada *et al.* modeled and compared mold cavity flow with the local EMBr and the ruler EMBr.[14] It was found that, although both types of EMBr lowered meniscus velocity and penetration depth, the ruler EMBr more effectively stabilized meniscus flow. Zeze *et al.* showed good comparison between a physical mercury model and a numerical model to illustrate that applying a ruler EMBr causes pluglike (nonrecirculating) flow with a relatively constant velocity to develop in the mold cavity.[15]

Flow-control–mold (FC-mold) electromagnetics span two thin, rectangular magnets across each wide face. One is located at the meniscus, and the other is located beneath the SEN ports.[12] This type of EMBr aims to control the fluid flow both exiting the nozzle and at the meniscus, and to control meniscus velocity. Hackl *et al.* used plant measurements to show that the use of an FC mold reduces meniscus fluctuations and surface defects on finished coils.[12] Idogawa *et al.* used numerical simulations to show that the FC mold decreases overall velocities in the mold cavity.[16] These results were confirmed with the use of a mercury model. Li *et al.* simulated flow in a caster with an FC mold while incorporating argon bubbling. It was found that the EMBr reduces the velocities of the bubbles, but does not significantly hinder bubble flotation.[17] While the FC mold is usually employed to decrease velocities at the meniscus,[12,16,17] it might also be able to increase meniscus velocity. A strong magnetic field across the mold below the SEN ports, combined with a weak or nonexistent magnetic field at the meniscus, could cause an upward deflection of the jets exiting the SEN and therefore a higher velocity at the meniscus.

This work focuses on quantifying the effect of a local EMBr and the variation of SEN submergence depth on steel flow in a typical continuous casting mold. In previous work, researchers have routinely made assumptions regarding how the EMBr field varies throughout the mold cavity.[13,14] For example, a local EMBr is often modeled as having a magnetic field strength which decreases linearly with radial distance from the point of maximum field strength, which is assumed to be the center point of the magnet used to create the field.[13,14] The magnetic field is typically neglected outside of the rectangular area enclosed by this magnet. In actuality, the accuracy of the flow computations depends on the accuracy of the EMBr field. In the present work, this accuracy is achieved by direct measurement of the EMBr field in the mold cavity.

Validation of numerical simulations with both analytical solutions and experimental results is needed to prove the numerical model is accurate. Only a few previous models have compared velocity predictions with measurements in experimental models.[10,16] In the present work, model validation is accomplished by comparison with a previous test problem and with both surface velocities and oscillation mark profile measured in the steel plant.

II. MODEL DESCRIPTION

In this work, a RANS model of turbulent fluid flow including electromagnetics is used to simulate the time-averaged flow pattern in a 90-mm-thick slab-casting mold with a local EMBr. Previous work has shown that RANS model predictions compare well with the time-averaged results obtained from both large eddy simulations and water-model measurements of turbulent flow in a similar continuous casting mold cavity.[18–20]

A. *Governing Equations*

The steady-state, incompressible, three-dimensional Navier–Stokes equations are solved in a nozzle and mold domain. The continuity equation for conservation of mass is

$$\rho(\nabla \cdot \vec{v}) = S_m \qquad [1]$$

where ρ is density, $\vec{v}$ is velocity, and S_m is a mass source/sink term used to model shell solidification. The equation for conservation of momentum is

$$\rho(\nabla \cdot (\vec{v}\vec{v})) = -\nabla p + \nabla(\mu_{\text{eff}}(\nabla \cdot \vec{v})) + \rho\vec{g} + S_{\text{mom}} + \vec{F} \qquad [2]$$

where p is pressure, S_{mom} is a momentum source/sink term used to model shell solidification, $\vec{F}$ is a momentum source/sink term used to incorporate the electromagnetic force, and μ_{eff} is the effective viscosity, calculated by

$$\mu_{\text{eff}} = \mu_o + \mu_t \quad [3]$$

where μ_o is the molecular viscosity and μ_t is the turbulent viscosity, as discussed subsequently.

Launder and Spalding's K-ε model is used to model turbulence,[21] which requires solving the following two additional transport equations to determine turbulent kinetic energy K and turbulent dissipation rate ε.

$$\rho(\nabla(K\vec{v})) = \nabla \cdot \left(\left(\mu_o + \frac{\mu_t}{\sigma_K}\right)\nabla K\right) + G_K - \rho\varepsilon \quad [4]$$

$$\rho(\nabla(\varepsilon\vec{v})) = \nabla \cdot \left(\left(\mu_o + \frac{\mu_t}{\sigma_\varepsilon}\right)\nabla \varepsilon\right) + C_1\frac{\varepsilon}{K}G_K + C_2\rho\frac{\varepsilon^2}{K} \quad [5]$$

where G_K represents the generation of turbulence kinetic energy due to the mean velocity gradients. It is defined as

$$G_K = -\rho\overline{u_i' u_j'}\frac{\partial u_j}{\partial x_i} \quad [6]$$

The turbulent viscosity can now be solved for using the following equation:

$$\mu_t = \rho C_\mu \frac{K^2}{\varepsilon} \quad [7]$$

The empirical constants are given as[22]

$$C_\mu = 0.09,\ \ C_1 = 1.44,\ \ C_2 = 1.92,\ \ \sigma_K = 1.0,\ \text{and } \sigma_\varepsilon = 1.3 \quad [8]$$

The magnetic induction method for solving for electromagnetic force is derived from Ohm's law and Maxwell's equation.[22] A magnetic field is induced when a conducting fluid, such as molten steel, moves through an applied magnetic field $\vec{B}_o$ with a velocity $\vec{v}$. This induced field $\vec{b}$ is calculated by solving

$$(\vec{v}\cdot\nabla)\cdot\vec{b} = \frac{1}{\mu\sigma}\nabla^2\vec{b}\cdot\left(\left(\vec{B}_o + \vec{b}\right)\cdot\nabla\right)\cdot\vec{v} - (\vec{v}\cdot\nabla)\cdot\vec{B}_o \quad [9]$$

The total magnetic field is then

$$\vec{B} = \vec{B}_o + \vec{b} \quad [10]$$

Current density can then be obtained through

$$\vec{j} = \frac{1}{\mu}\nabla \times \vec{B} \quad [11]$$

The Lorentz force, or induced electromagnetic force, is determined using

$$\vec{F} = \vec{j} \times \vec{B} \quad [12]$$

This force term is subsequently added into the momentum equations as a source/sink term.

The meniscus height was calculated using the following approximation based on potential energy[20]

$$\text{Meniscus height} = \frac{P_{\text{static}} - \overline{P}_{\text{static}}}{\left(\rho_{\text{steel}} - \rho_{\text{slag}}\right)\times\vec{g}} \quad [13]$$

where ρ_{slag} is slag density, P_{static} is static pressure at each point, and $\overline{P}_{\text{static}}$ is the average static pressure over the top surface of the mold domain.

The governing equations are discretized in FLUENT using an implicit, first-order upwinding scheme and the SIMPLE algorithm for pressure-velocity coupling.[22] FLUENT's segregated solver is used to solve the discretized equations in the following order. Initial conditions (if calculating the first iteration) or values from the previous iteration step are used to solve for the velocities in each cell using the conservation of momentum equations. The continuity equation is then imposed to correct any mass-flow imbalances present in the cells. Turbulence equations are subsequently solved for K and ε, followed by the electromagnetic equations for the Lorentz force using the magnetic induction method. The calculated Lorentz force is then added into the momentum equations as a source term at the next iteration step.

B. *Nozzle and Mold Flow Parameters*

To ease convergence, the nozzle and the mold cavity domains were modeled separately, with the flow at the outlet of the nozzle being prescribed as the flow at the inlet of the mold cavity. Hershey *et al.* showed that results using this approach match well with results of simulations of the combined nozzle and mold cavity domains.[23]

The simulated nozzle has two 45-deg downward-angled, oversized, rectangular ports as shown in Figure 1. The entire nozzle was modeled, starting from just below the stopper rod. The mesh was comprised of about 200,000 hexahedral cells, and can be seen in Figure 2. Because three separate SEN depths were studied, three separate mold cavities were meshed. To reduce computational cost, one quarter of each mold cavity was modeled, taking twofold symmetry into account. The mold domains were curved to model only the liquid region, adding mass and momentum sinks at the shell boundaries to extract fluid across the solidification front. The shell thickness was calculated using CON1D,[24] and the curves representing this thickness as a function of depth into the mold cavity on both the wide and narrow faces are shown in Figure 3. Figure 4 shows a mold cavity mesh near the mold inlet.

One nozzle and nine mold cavity flow simulations were performed. Table I(a) lists the common simulation conditions, and Table I(b) shows the remaining conditions that differentiate each case.

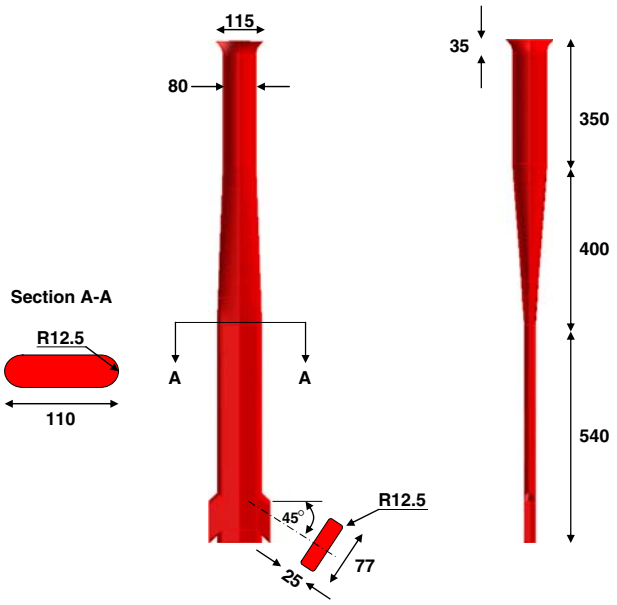

Fig. 1—Nozzle geometry.

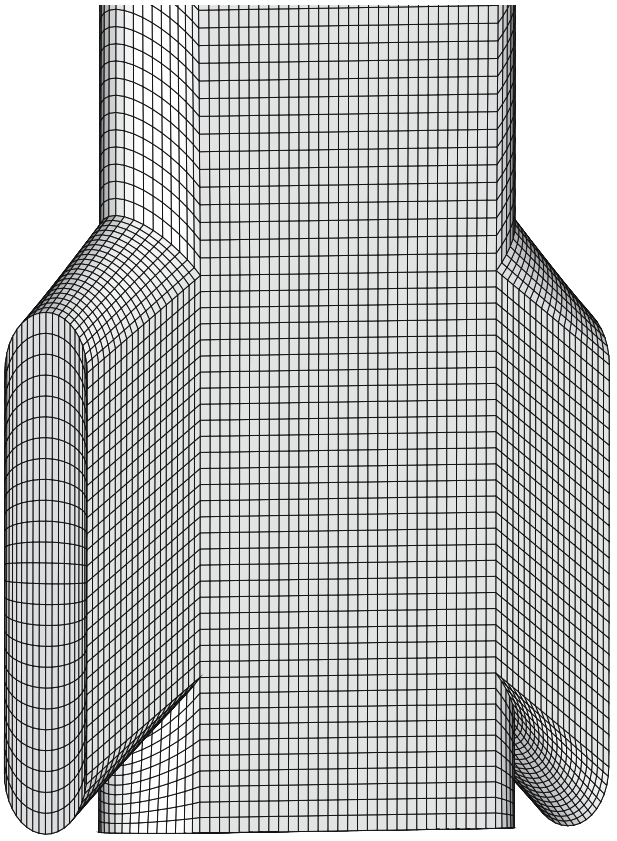

Fig. 2—Nozzle mesh in lower SEN region.

C. *Boundary Conditions*

(1) Nozzle inlet: It was assumed that a fully developed velocity profile was present at the nozzle inlet. Standard equations for fully-developed flow in a pipe were used to prescribe this profile.[25] Values of K and ε were both set to arbitrary small values, $10^{-4}\ m^2/s^2$ and $10^{-4}\ m^2/s^3$, respectively, to allow turbulence to develop naturally.

(2) Mold cavity inlet: The velocity and turbulence parameters at the mold cavity inlet are specified using the results calculated at the outlet plane of the port from the nozzle simulation. A text file containing the nozzle right port velocity, K, and ε values at each node was written. This file was then read into FLUENT and the values were used as the inlet conditions for the mold cavity simulations.

(3) Nozzle and mold cavity outlets: Bai *et al.* showed that using pressure boundary conditions allows for an accurate flow simulation, including the velocities near the outlet boundaries.[26] These outlet conditions allow recirculation zones to appear at the outlets, which has a large effect on flow in the domain. Gage pressure at both the nozzle and the mold cavity outlets was set to zero, which is an arbitrary value that acts as a reference pressure for the rest of the domain. Outlet values of K and ε were set to $10^{-4}\ m^2/s^2$ and $10^{-4}\ m^2/s^3$, respectively.

(4) Walls: A no-slip condition and standard wall laws[22] were applied on the inner walls of the nozzle in the nozzle simulation and the exterior walls of the nozzle, top surface, and shell boundaries in the mold cavity simulations. The gradients of all electromagnetic variables are equal to zero at all walls, which are assumed to be stationary. Exceptions to these conditions for selected wall areas are defined subsequently.

(5) Mold cavity top surface: A zero-shear condition is specified at the top surface, which assumes the effect of the mold flux is negligible. Standard wall laws are used.

(6) Shell boundaries: To simulate the continuous extraction of the solidifying steel shell, the shell wall boundaries are given a downward velocity equal to the casting speed.

(7) Mass/momentum sink cells: The method of extracting mass and momentum to model the

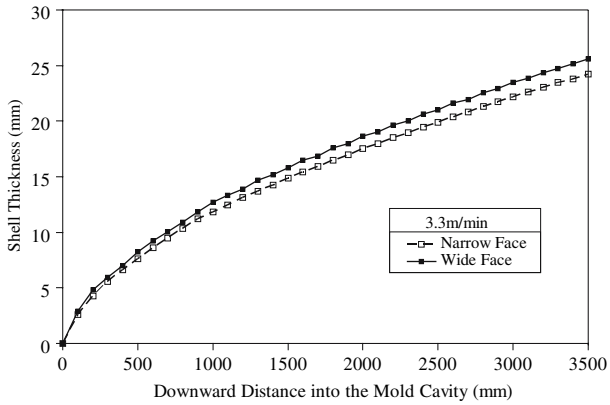

Fig. 3—Shell thickness profiles calculated using CON1D[24] used to define liquid cavity shape.

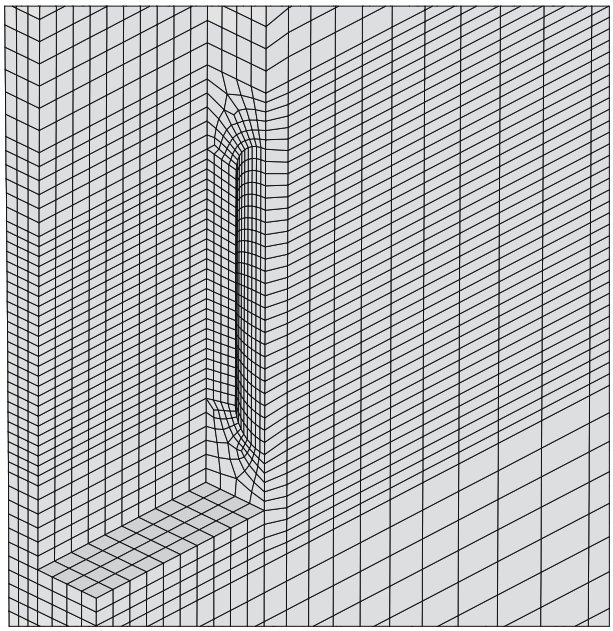

Fig. 4—Mold cavity mesh near inlet.

Table I(a). Simulation Parameters for All Cases

Casting speed	3.3 m/min
Mold width	1374 mm
Mold thickness	90 mm
Meniscus level Below top of mold	100 mm
Domain width	687 mm
Domain thickness	45 mm
Domain length	2500 mm
ρ_{steel}	7000 kg/m^3
ρ_{slag}	3000 kg/m^3
μ	0.006 kg/ms
σ	714,000(Ω m)$^{-1}$
Gravity	9.81 m/s^2

Table I(b). Simulation Parameters: Variations by Case

Case	SEN Depth (mm)	EMBr Setting (T)
Case 1	250	0
Case 2	250	0.2525
Case 3	250	0.355
Case 4	300	0
Case 5	300	0.2525
Case 6	300	0.355
Case 7	350	0
Case 8	350	0.2525
Case 9	350	0.355

solidification of steel into the shell is explained by Rietow.[25] In this method, thin (1.0-mm-thick) cells are created along the faces of the boundaries representing the interface between the liquid and the solidifying shell. The curvature of the shell is then used to calculate the amount of mass and momentum removed at each cell location. This is implemented in FLUENT using a user-defined function (UDF), which adds these mass and momentum sinks to their respective governing equations.

(8) Magnetic field: The magnetic field, $\vec{B}_o$ (T), measured at Nucor Steel was imported in and applied to the fluid domain.
(9) Symmetry: At the two planes of symmetry on the mold domain centerplanes, normal velocities, as well as all gradients, are equal to zero.[22]

All computations were performed on a PC with a 2.8 GHz dual-core Intel Pentium IV processor and 2.0 GB RAM. The nozzle simulation converged in about 4 hours and required approximately 1100 iterations. The mold cavity simulations without the EMBr converged in about 5 hours and required approximately 3700 iterations each, while the mold cavity simulations with the EMBr required about 24 hours and 20,000 iterations each to reach convergence.

III. EXPERIMENTAL PROCEDURES AND RESULTS

Plant measurements were obtained on the South slab caster at Nucor Steel (Decatur, AL). This caster features a standard two-port SEN and a 90-mm-thick, straight, parallel mold with a sinusoidal oscillator. A local EMBr is used on this caster and was set to 0.355 T at the time of the experiments. Table I gives the casting conditions for each of the following experiments.

A. *EMBr Field Measurement*

A Gauss meter[27] was used to measure two different EMBr fields (0.2525 and 0.355 T) in the mold cavity without molten steel. At every 10 cm across the center of the mold cavity measurements were recorded, lowering the probe downward in 5-cm increments. Measurements started 2 cm below the top of the mold and extended to a depth of 72 cm into the mold cavity, spanning the width of the mold up to 2 cm from either narrow face. Magnetic field strength across the thickness of the mold was measured to vary by a maximum of 3 pct, so it was neglected.

Figure 5(a) shows a contour plot of the measured EMBr field for the nominal field strength of 0.355 T, along with the location of the magnets that create the field. Notice that although the magnitudes of the magnetic fields are about the same on each mold half, the directions are opposite. The maximum field strength is 0.32 T at the center of each coil, which decreases with radial distance. These results clearly show that the magnetic field extends far beyond the boundaries of the magnets and is present in the entire upper mold region. The scalability of the measured magnetic field is tested by linearly scaling the measured 0.355 T field down to 0.2525 T. A comparison of the measured and scaled 0.2525 T field is shown in Figure 5(b). The field scales well near the narrow faces and the center of the mold. However, in-between where the field strength is largest, the magnitude of the measured field is somewhat larger than expected from scaling. Perhaps this is due to inaccurate display of the field setting at the caster.

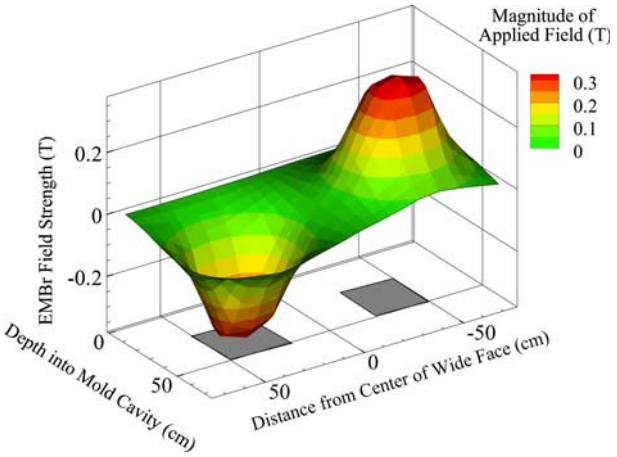

(a)

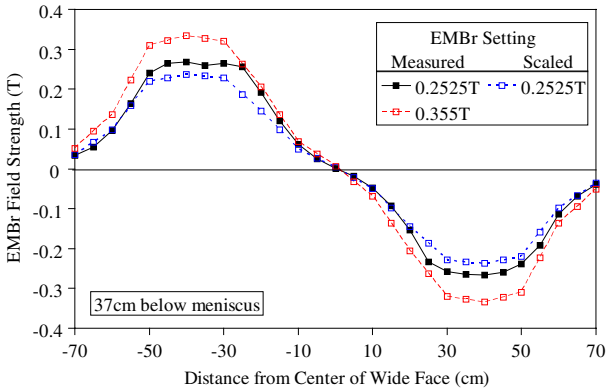

(b)

Fig. 5—(*a*) Contours of measured electromagnetic field strength for 0.355 T setting; hatching indicates physical location of EMBr magnets. (*b*) EMBr field strength profiles for two settings along a wide-face centerline 37 cm below the meniscus, comparing measurements and estimate from simple scaling.

B. *Nail Board Dip Test*

The nail board dip test is a method of characterizing flow at the meniscus. The test is performed by inserting a number of nails into a long board and dipping them perpendicularly into the top surface of the molten steel for 3 to 5 seconds. Upon removal, a knob of steel has solidified on the end of each nail. Nail board dip tests have commonly been used to determine the depth of the liquid flux layer that lies atop the molten steel.[28] This can be found by affixing aluminum wire alongside the nails prior to performing the dip test, and recording the difference between the melted wire height and the solidified knob.

The angular profile of the knob can be further analyzed to gain insight into the flow pattern. The direction of the flow can be found by recognizing that the high end of the angular knob profile represents the direction from which steel impinges on the nail. Recently, Rietow used a carefully validated computational model to determine a relation to correlate knob height difference and nail diameter to surface velocity of the molten steel across the top of the mold.[25] Knob

Fig. 6—Result of nail board dip test showing solidified lumps, which reveal surface velocity.

height difference is the difference in height between the low and high ends of the knob profile. This correlation allows for an accurate and fast measurement of meniscus velocity in a plant setting, which is compared with computational results in the current study for validation purposes.

Ten 7.5-cm-long, 5-mm-diameter nails were hammered into a 6.2-cm-wide, 2-cm-thick, 550-cm-long pine board to a depth of approximately 2.5 cm. The nails were spaced 5 cm apart and 5 cm from each end of the board. Note that the width of the board is about 15 cm less than the width of the mold to ensure that the board and nails do not interfere with the steel shell or SEN upon insertion into the mold cavity. The nails were then dipped into the mold cavity for approximately 4 seconds, removed, cooled, and measured. The nail board resulting from this test can be seen in Figure 6. The knob height difference can be noticed most easily near the narrow face, where velocities are the highest.

C. *Oscillation Mark Profiles*

Oscillation marks are small depressions in the surface of every steel slab caused by the partial freezing of the meniscus during a mold oscillation cycle.[29] These marks reveal the shape of the meniscus at the instant they formed. This gives another opportunity to validate the computational model; the simulated meniscus shape caused by the fluid flow pattern can be compared with the meniscus shape obtained from oscillation marks. Figure 7 shows a photograph of oscillation marks traced on a sand-blasted surface of a sample of steel slab.

IV. MODEL VALIDATION WITH TEST PROBLEM

Many previous studies have shown that solving three-dimensional single-phase RANS equations and the K-ε turbulence model with FLUENT gives results that compare well to both time-averaged LES simulations and water model measurements.[5,19] The fluid-flow model is thus assumed to be accurate.

To validate the Lorentz force and coupling equations using the FLUENT magnetohydrodynamics (MHD) module, a simple test simulation was performed. The specific test problem and experimental measurements were provided by Moreau.[30] The geometry consists of a 704-mm-long, 40-mm-high, 2-mm-thick channel with a constant magnetic field applied uniformly over a 304-mm-long rectangular region near its center. Material properties and boundary conditions are given in Table II.

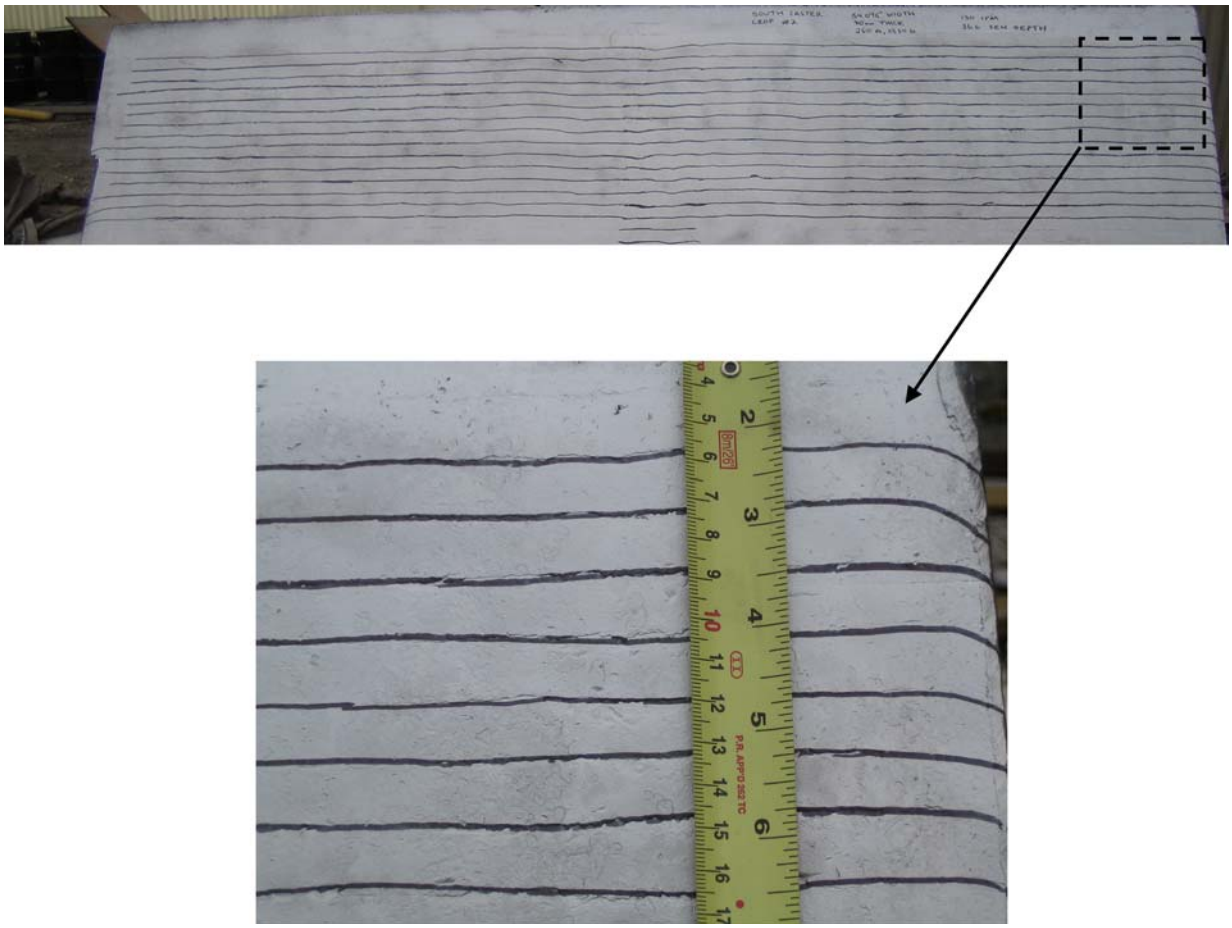

Fig. 7—Oscillation marks on slab surface reveal liquid surface profile at meniscus.

Table II. Conditions for MHD Test Case

Domain length	704 mm
Domain height	40 mm
Domain thickness	2 mm
EMBr region length	center 304 mm of domain
EMBr strength	1.3482 T
ρ	13550 kg/m^3
μ	0.00155825 kg/ms
σ	1.05×10^6 $(\Omega\ \text{m})^{-1}$
v_{inlet}	1.16141 m/s
K_{inlet}	5.99×10^5 m^2/s^2
$\varepsilon_{\text{inlet}}$	7.529×10^5 m^2/s^3
$P_{\text{gage, outlet}}$	0 MPa

Figures 8(a) and (b) show vectors of Lorentz force for this problem calculated previously by Cho[31] and currently with FLUENT, respectively. The magnetic field induces a Lorentz force, which appears at the edges of the magnetic-field region and opposes the flow. The vectors of Lorentz force qualitatively match well with the previous numerical results.

Quantitative analysis of the flow results was performed by comparing velocity profiles along the vertical centerline of the domain. Figure 9 shows that the current profiles match well with the previous computations[31] and measurements.[30] An ''M-shaped'' profile is observed, with high velocities near the walls and relatively low velocities near the center of the channel. Because the results of this test problem agree with previously obtained numerical and experimental results, the fluid flow modeling procedure including the coupled effects of the applied electromagnetic field is assumed to be accurate for all simulations in this work.

V. TYPICAL RESULTS AND VALIDATION WITH CASTER EXPERIMENTS

To further validate the model, a simulation was performed using the conditions under which the experimental nail-board and oscillation-mark measurements were collected (case 6 in Table I). The flow fields also represent typical results for this continuous-casting nozzle and mold cavity.

A. *Nozzle Flow*

Velocity is relatively constant throughout the top half of the nozzle. However, this velocity doubles in magnitude (0.8 to 1.6 m/s) as the nozzle's cylindrical cross section tapers into a thin, rectangular cross section. Figure 10 shows velocity vectors on a plane through the

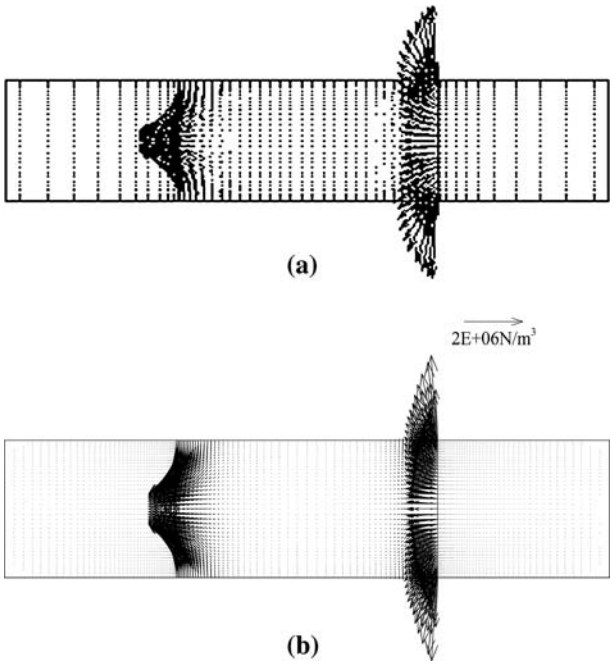

Fig. 8—Vectors of Lorentz force on the domain centerplane for the MHD test case: (*a*) results from Cho[31] and (*b*) results of this work.

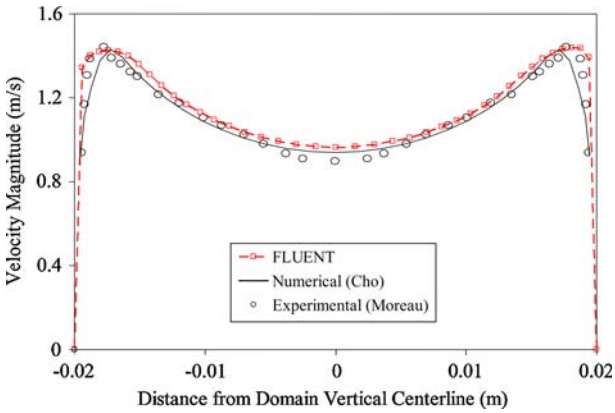

Fig. 9—Comparison of velocity profiles along a vertical line at the horizontal center of the MHD test case domain.

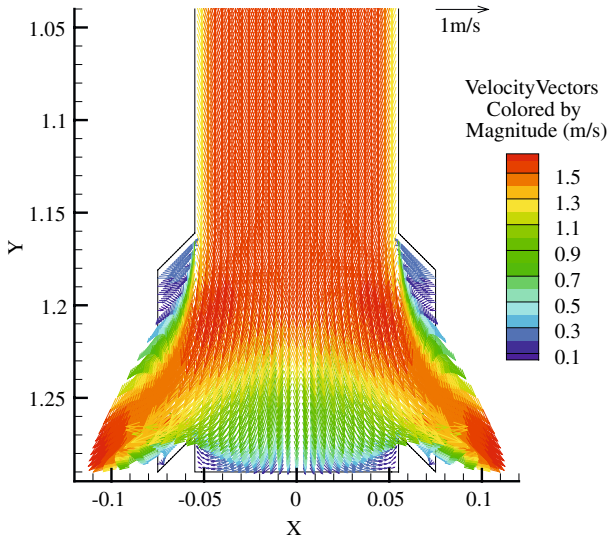

Fig. 10—Nozzle velocity vectors on wide face centerplane.

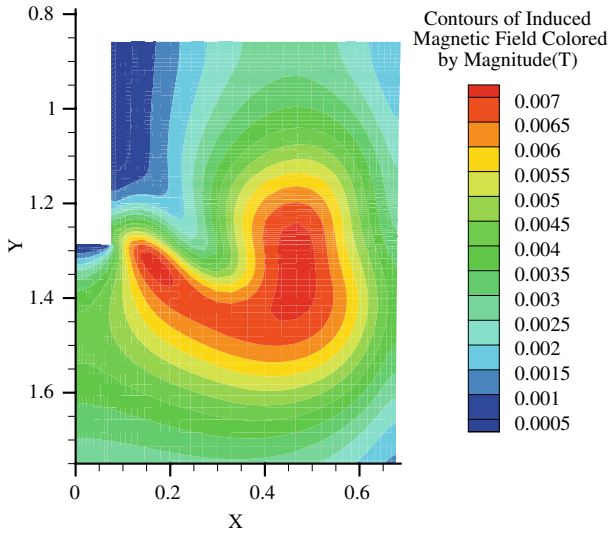

Fig. 11—Contours of induced magnetic field for case 6.

center of the width of the lower SEN region. High velocity is maintained throughout the lower half of the nozzle until the flow exits the ports. Recirculation regions at the top and the bottom of the port exhibit low velocities where fluid re-enters the nozzle. This recirculation might be beneficial, as it helps to prevent nozzle clogging.[32] Flow in the well region also exhibits recirculation, as the downward central jet impacts and flows along the well bottom and back over the lip to join the main jets leaving the ports. In this way, the well helps to stabilize the turbulent flow, which tends to oscillate chaotically about this time-averaged flow pattern.

B. *General Mold Cavity Flow Pattern*

Figure 11 shows the induced magnetic field for case 6, which is created by the conducting steel flowing through the applied magnetic field. According to Eq. [9], the magnitude of the induced field is proportional to the speed in the mold cavity and the applied field. Therefore, the induced field is largest just beyond the SEN ports, where the largest velocities in the mold cavity enter the region of the applied field. The induced field strength then lowers as the jet moves through the applied field, dissipates, and impinges on the narrow face. Note that the maximum magnitude of the induced field (0.007 T) is just 2 pct of the maximum value of the applied field (0.32 T). Thus, the induced field does not have a significant impact on flow in the mold cavity and the coupling effect of the flow equations on the electromagnetic equations is small.

Vectors of Lorentz force along the wide face centerplane are plotted in Figure 12. Large Lorentz forces, which oppose the flow, can be seen where the jet encounters the regions of strong magnetic field.

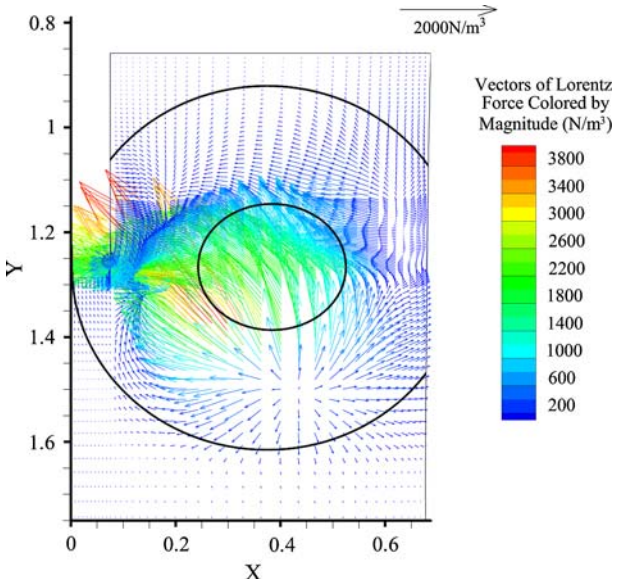

Fig. 12—Vectors of Lorentz force on the mold wide face centerplane for case 6 with outer inscribed circle showing extent of EMBr field and inner oval showing region of strongest field.

Figures 13(f) and 14 show streamlines and velocity vectors on the wide face centerplane, respectively, for case 6. The jet exiting the nozzle travels across the mold cavity and, upon impingement on the narrow face, splits into upward and downward flowing "secondary" jets. This diverted flow creates the classic upper and lower recirculation zones of a double-roll flow pattern. In the upper recirculation zone, fluid flows up the narrow face, back across the top surface, and down the SEN wall to rejoin the jet exiting the nozzle. The brake causes some of the secondary jet flowing up the narrow face to split off early and flow back across the mold just above the brake region, altering velocities in the upper recirculation region. In the lower recirculation zone, fluid flows down the narrow face, across the mold cavity width, and up the center of the mold cavity. The lower recirculation zone is much larger and has lower velocities than the upper zone because it is not confined. The upper zone is constrained by the top surface and the jet exiting the SEN, which tends to bend the jet slightly upward.

Flow behavior near the top surface can be seen in Figure 15, which shows velocity vectors on a plane 10 mm below the meniscus. The flow is uniform, except for swirling near the SEN. Velocity toward the SEN on a line across the wide-face centerplane 10 mm below the meniscus is included in Figure 16. A parabolic velocity profile is observed, with a maximum about 450 mm from the center of the mold cavity.

Figure 17 shows downward velocity profiles at various distances below the meniscus on a line across the wide-face centerplane. At 0.5 m below the meniscus, velocity is upward (negative) near the center of the mold cavity, indicating upward flow beneath the SEN. Velocity is downward (positive) in the central region of the

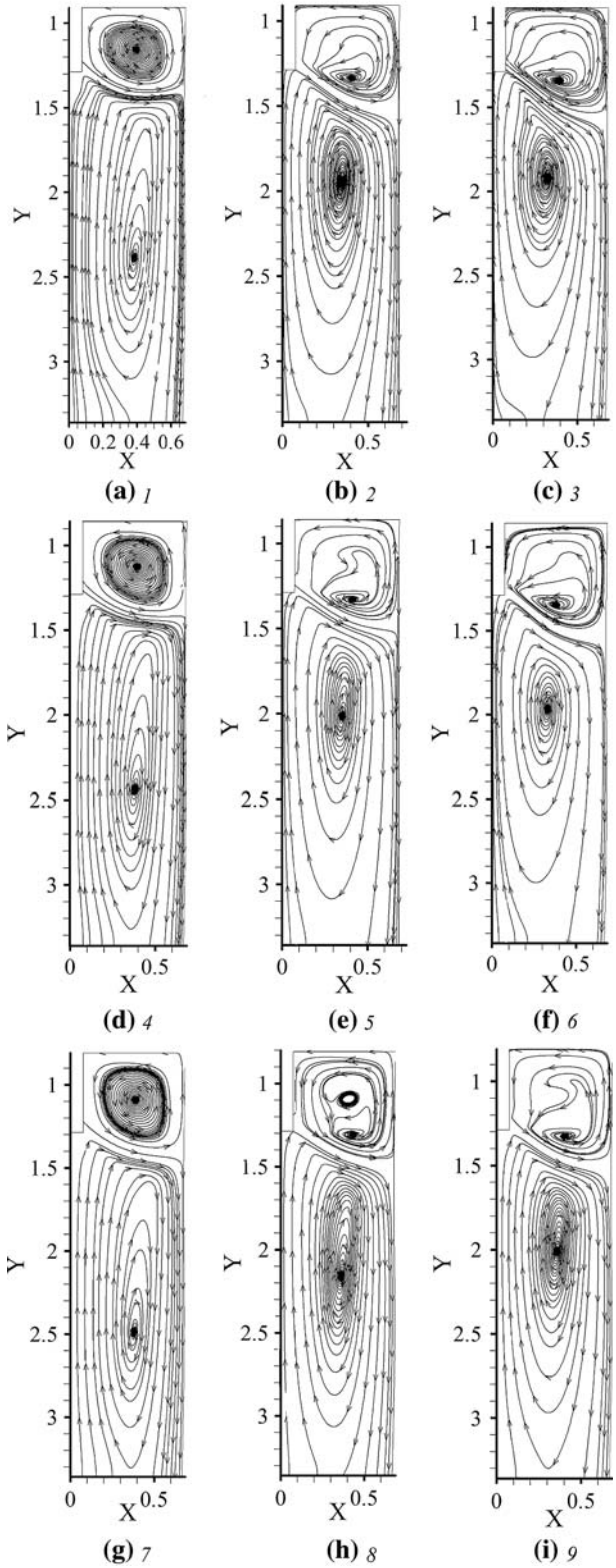

Fig. 13—(*a*) through (*i*) Streamline plots on mold wide face centerplane for cases 1 through 9, respectively.

wideface (150 to 400 mm), where the jet is located. Velocity is upward (negative) again along the narrow face. At 1.0 and 1.5 m below the meniscus, the velocity

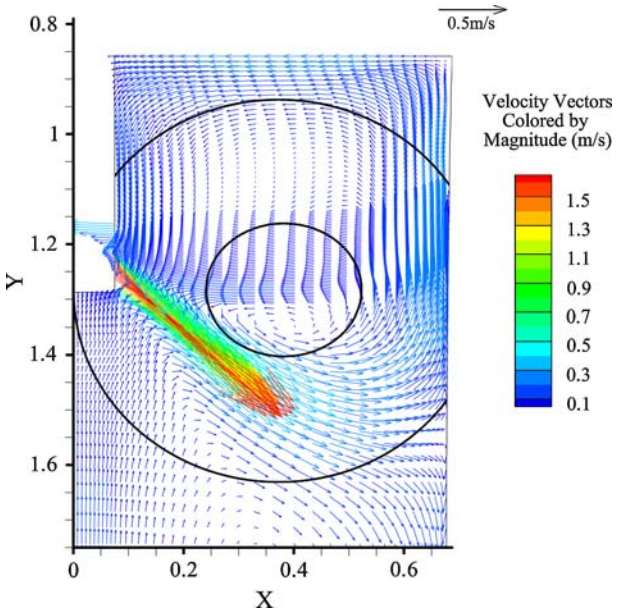

Fig. 14—Velocity vectors on the mold wide face centerplane for case 6, with outer inscribed circle showing extent of EMBr field and inner oval showing region of strongest field.

profiles are very similar. Velocity is upward beneath the SEN and downward near the narrow face. The velocity magnitudes are smaller, which is typical of the large, weak lower recirculation zone.

Figure 18 shows the meniscus profile along the outer edge of the wide face. Flow up the narrow face raises the surface level there. The surface level dips in the middle region of the mold. A 5.26-mm standing wave is observed, which is defined as the minimum meniscus height subtracted from the maximum meniscus height.

C. *Validation Using Nail Boards*

Using the correlation by Rietow,[25] the nail board dip test was used to estimate meniscus velocity. Zoomed photographs of each nail were taken, along with a ruler for scaling, and knob height difference was measured. Table III documents each knob height difference and its corresponding surface velocity. Velocities at each nail are plotted across the mold in Figure 19, which also

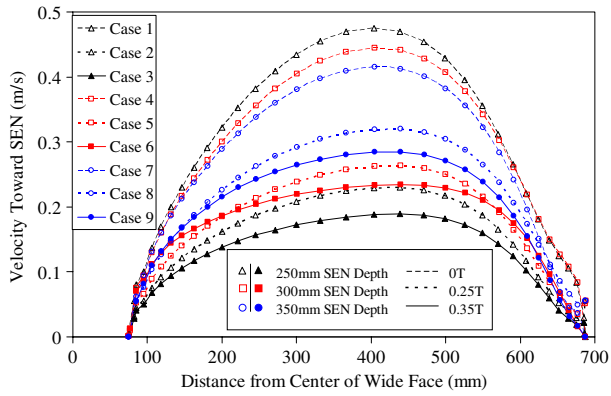

Fig. 16—Velocity toward the SEN on a line across the wide face centerplane 10 mm below the meniscus for all cases.

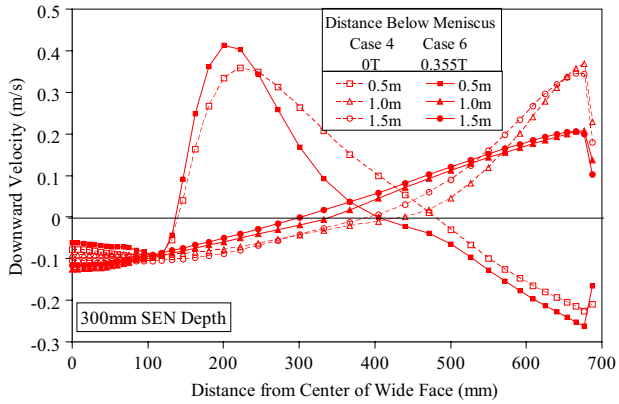

Fig. 17—Effect of electromagnetic field on downward velocity profiles at various distances below the meniscus (cases 4 and 6).

shows the model calculated surface velocity profile for the same conditions (case 6). The numerical results match surprisingly well both near the narrow face and near the SEN. Negative velocity is measured for one nail near the center of the meniscus, which suggests that flow was swirling or flowing toward the narrow face at that point. This transient effect cannot be simulated by the steady-state model. Both the shape of the velocity profile and the magnitude of the velocities are consistent between the two plots.

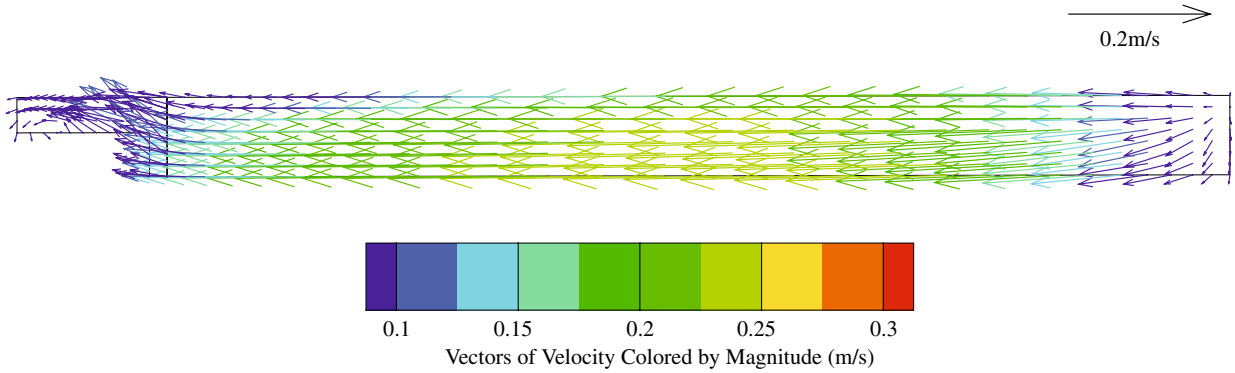

Fig. 15—Velocity vectors on a plane 10 mm below the meniscus.

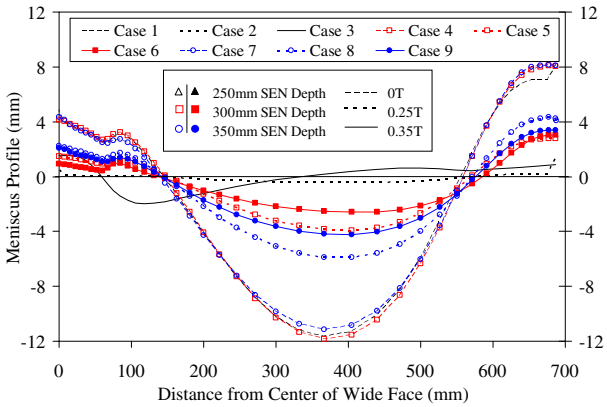

Fig. 18—Meniscus profiles along the wide face outer edge for all cases.

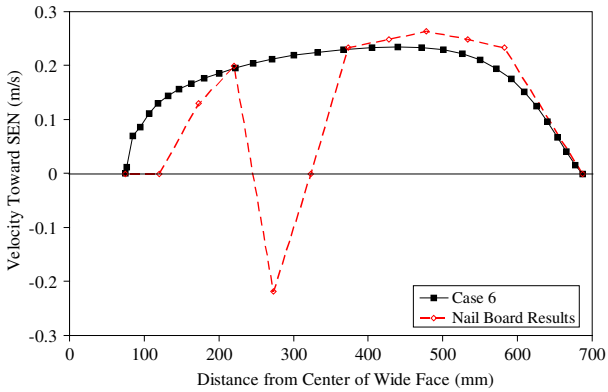

Fig. 19—Comparison of top-surface velocities obtained from computations and measurements.

Table III. Correlation of Knob Height Difference to Meniscus Velocity

Nail Distance from Narrow Face (mm)	Knob Height Difference (mm)	Velocity toward the SEN (m/s)
117	2	0.23
167	2.5	0.25
217	3	0.26
267	2.5	0.25
317	2	0.23
367	0	0
417	−1.5	−0.22
467	1	0.20
517	0.5	0.13
567	0	0

D. *Validation Using Oscillation Marks*

Validation with experimental data was also obtained by comparing the oscillation marks observed on the finished steel slab with the calculated meniscus profiles found using FLUENT for the same casting conditions (case 6). Figure 20 compares the calculated meniscus profile with eight separate oscillation marks. The oscillation marks were placed on the graph such that the total "area under the curve" of each oscillation mark is equal to zero. The shape of the calculated profile roughly matches that of the oscillation marks. The trend of a high wave at the narrow face that slopes downward and stabilizes about halfway across the wide face before sloping slightly upward near the SEN is witnessed in both the experimental and numerical cases. The scale of the numerically-calculated profile also matches that of the oscillation marks. One reason there is not exact matching is that the oscillation marks are transient by nature: one mark is made during each mold oscillation cycle. This transience is indicated by the variations between the eight oscillation marks.

Table IV lists the standing wave height of each measured oscillation mark, the average of all eight, and the corresponding computational result (case 6). The variations due to transient turbulent flow are seen again, as the standing wave heights range from 2.25 to 6.0 mm. The average measured height is 4.41 mm, which is only 0.85 mm smaller than the calculation. This shows that the model can roughly predict the average surface profile, both qualitatively and quantitatively, which is the best that can be expected from a steady-state model.

VI. PARAMETRIC STUDY

A. *Increasing EMBr Strength*

Cases 4, 5, and 6 simulate mold cavity flow at a 300-mm SEN depth for EMBr field strengths of 0, 0.253, and 0.355 T, respectively. Figures 13(d) through (f) show streamlines on the wide-face centerplane for each case. Increasing EMBr field strength causes a dramatic change in the flow pattern. The most obvious difference is the direction of the jet exiting the SEN and its impingement point on the narrow face. With no field (case 4), the jet travels almost straight across the mold cavity. The jet traverses directly through the applied field region in cases 5 and 6. Because the jet wants to flow through that region, applying the EMBr in cases 5 and 6 induces a large Lorentz force to oppose the flow. This Lorentz force increases as magnetic field strength increases. To conserve mass and momentum, the jet simply deflects downward, away from the center of the strong magnetic field. This bending of the jet steepens its angle, so that it impinges deeper onto the narrow face. Further increase in magnetic field strength causes a larger downward deflection of the jet. Although it bends downward, the jet still passes through the bottom left corner of the region of high magnetic field, which dissipates and slows the jet. Due to the steeper downward jet with lower velocity, lower momentum, and deeper impingement, the upper recirculation zone greatly weakens when the field is applied (cases 5 and 6).

This weakening of the upper recirculation zone lowers the top-surface velocity profiles, as shown in Figure 16. Surface velocity decreases as EMBr field strength increases. Lowering surface velocity below ~0.4 m/s lessens the chance of mold-slag entrainment, which demonstrates one of the benefits of using EMBr. Figure 17 compares downward velocity profiles for 0 and 0.355 T cases at various distances below the meniscus. Downward velocity at 0.5 m below the

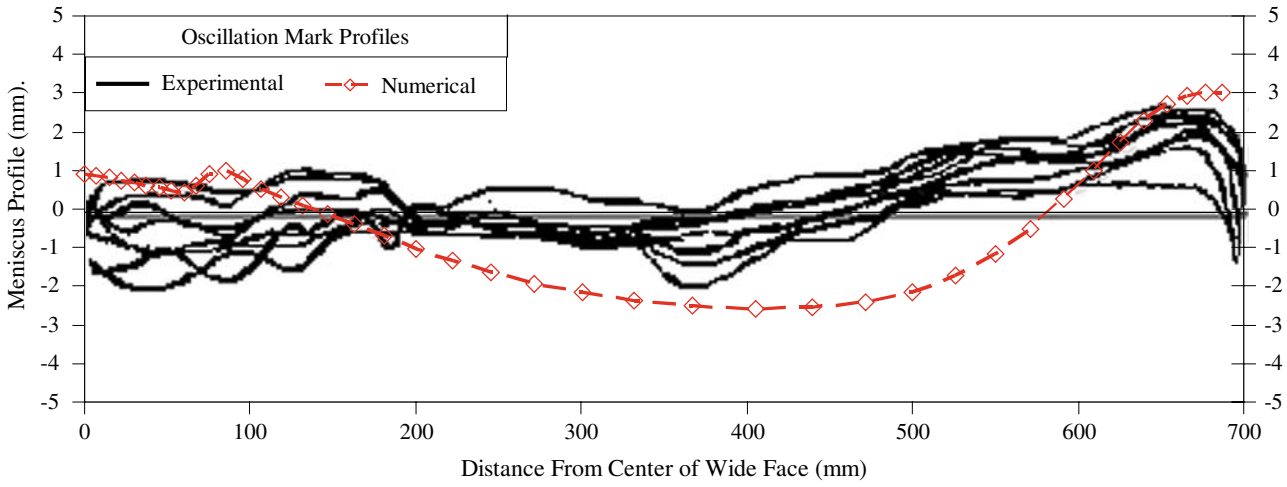

Fig. 20—Comparison of calculated meniscus profile from case 6 with oscillation marks.

Table IV. Oscillation Mark Standing Wave Height

Oscillation Mark	Standing Wave Height (mm)
1	3.75
2	5.25
3	6.0
4	4.0
5	2.25
6	4.0
7	4.25
8	5.75
Average	4.41
CFD result (case 6)	5.26

meniscus increases as EMBr field strength increases, due to the downward deflection of the jet.

However, at 1.0 m below the meniscus a different trend is observed. Maximum downward velocity, which is found near the narrow face, decreases as EMBr field strength increases. The increase of EMBr field strength also flattens the velocity profile and equates regions of upward flow (beneath the SEN) and downward flow (near the narrow face). This is indicative of a wide, relatively weak recirculation zone compared to the narrow recirculation zone seen without the EMBr. The same trends are seen at 1.5 m below the meniscus, though the region of upward flow at this depth is smaller than that seen at 1.0 m below the meniscus. This shows that the recirculation zone decreases in size as depth into the mold cavity increases. This reduces the penetration depth of possible inclusions, which can cause defects in the final product if entrapped.[3] It can be seen in Figure 18 that as EMBr field strength increases, meniscus wave height shrinks. Increasing EMBr field strength thus causes the top surface to flatten.

B. *Increasing SEN Depth without EMBr*

Cases 1, 4, and 7 simulate mold cavity flow without EMBr for 250-, 300-, and 350-mm SEN depths, respectively. Figures 13(a), (d), and (g) show streamlines on the wide face centerplane for each case. At the 250-mm SEN depth, the jet exits the SEN at 45 deg downward and flattens out as it crosses the mold cavity width. The jet also bends upward near the narrow face. This is caused by the lower pressure in the upper recirculation zone, due to this region being constrained between the upper surface and the jet. The jet stays fairly consistent with minimal diffusion and impacts almost straight onto the narrow face with relatively high velocities. Much of the flow deflects upward so the upper recirculation zone is strong with high velocities observed in the fluid moving upward along the narrow face, across the meniscus, and downward along the SEN walls.

Increasing SEN depth changes how the jet passes through the mold cavity. At 350-mm depth, the jet is steeper downward and more diffuse than at the 250-mm SEN depth. This causes less flow to deflect into the upper recirculation zone, so surface velocities are lower.

It is shown in Figure 16 that velocity across the top surface decreases as SEN depth increases. However, the effect is relatively small for constant field strength. Figure 21 shows that downward velocity at 1.0 m or more below the meniscus is similar for different SEN depths. Increasing SEN depth slightly increases downward flow near the narrow face, as more flow is directed into the lower recirculation zone. This could be detrimental by carrying more inclusions deep into the mold cavity, where they can become entrapped into the solidifying shell.

Figure 18 shows the meniscus profile (naturally plotted along the outer edge of the wide face) for each case. Without EMBr (cases 1, 4, and 7), the profiles are severe, showing 20-mm wave height across the mold. However, the effect of SEN depth is very small, which matches observations by Creech.[33]

C. *Increasing SEN Depth with EMBr*

With EMBr, the effect of SEN depth depends greatly on the jet location relative to the maximum braking region. Cases 3, 6, and 9 simulate mold cavity flow with 0.355 T EMBr field strength for 250-, 300-, and 350-mm

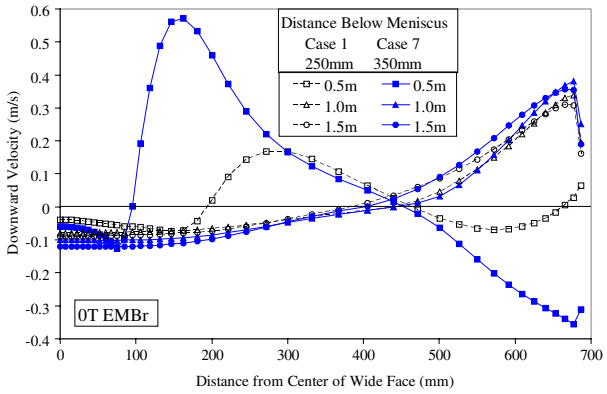

Fig. 21—Effect of SEN depth on downward velocity profiles for cases 1 and 7 without EMBr at various distances below the meniscus.

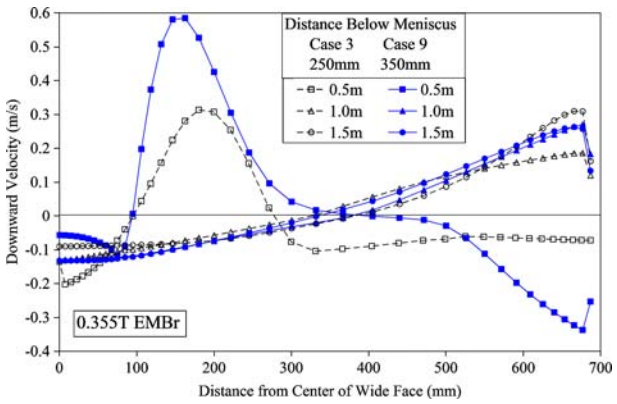

Fig. 22—Effect of SEN depth on downward velocity profiles for cases 3 and 9 with EMBr at various distances below the meniscus.

SEN depths, respectively. Figures 13(c), (f), and (i) show streamlines on the wide face centerplane for each case. With EMBr the effect of SEN depth changes. Raising the SEN brings the jet closer to the the center of the EMBr region, thereby increasing the EMBr effect. At the shallow 250-mm SEN depth, the jet exits the SEN at 45 deg down and flows directly through the region of highest applied magnetic field. This subjects the jet to the maximum braking force, which diffuses the flow, deflects the jet deeper, and causes the weakest upper recirculation zone. The result is slow flow across the meniscus (Figure 16).

Increasing SEN depth (*e.g.*, to 350 mm) sends the jet below the maximum braking region. This causes smaller Lorentz forces to act upon the flow field at deeper SEN depth. Thus, the jet experiences less dissipation and little downward bending as it crosses the mold cavity. The jet retains more velocity and momentum, causing more flow up the narrow face and increasing the intensity of the upper recirculation zone. As SEN depth increases, the jet passes farther below the strong area of applied magnetic field.

With EMBr, Figure 16 shows that top surface velocity increases as SEN depth increases. Figure 22 shows that downward velocity at locations below the SEN increases with increasing SEN depth, because the jet is less altered and thus carries more momentum and velocity into the lower recirculation zone.

Figure 18 shows of the effect on meniscus profile. With EMBr, the meniscus wave height increases as SEN depth increases. The increase of velocity and momentum into the upper recirculation zone caused by the less-altered jet at deep SEN depths causes more pressure variation at the meniscus.

VII. IMPLICATIONS

This investigation provides insight into how to best operate this caster. The local EMBr is beneficial, as it lowers surface velocity and flattens the meniscus profile (wave height). This prevents excessive surface velocities and the corresponding slag entrainment, level fluctuations, inclusions, and surface defects that accompany casting without electromagnetics for this geometry and casting speed. The EMBr field strength should vary with SEN depth in order to maintain constant meniscus conditions. Higher EMBr field strength is needed with deeper SEN submergence. Specifically, the field strength should increase from ~0.25 to 0.35 T as submergence increases from 300 to 350 mm, in order to maintain surface velocity at ~0.3 m/s and a stable meniscus wave height of ~7 mm.

VIII. SUMMARY AND CONCULSIONS

Fluid flow in a continuous casting nozzle and mold cavity under a local EMBr can be investigated quantitatively using FLUENT. The EMBr field at Nucor Steel in Decatur, AL was measured for use in the mold cavity simulations. The model and solution method were validated by comparing the results of a test case with previous experimental and numerical data. The results were also validated by comparing plant measurements of surface velocity from nail boards and meniscus shape (standing wave height) from oscillation mark profiles. A parametric study was conducted on the combined effects of EMBr and SEN depth, with the following findings.

1. The induced magnetic field is only ~2 pct of the applied magnetic field, so should not require two-way coupling with the fluid flow solution.
2. Increasing EMBr field strength at constant SEN depth causes the following: (a) steepening of the jet angle; (b) increasing jet impingement depth; (c) expanding the upper recirculation zone; (d) weakening the upper recirculation zone; (e) decreasing top surface velocity; (f) decreasing standing wave height at the meniscus; (g) deepening penetration of the jet into the lower recirculation zone; (h) increasing jet dissipation, which reduces downward velocity along the narrow face and flattens velocity profiles at depths of 1.0 m or more into the mold cavity.
3. Increasing SEN depth without EMBr has almost the same effects as increasing EMBr listed above. The only exception is that jet dissipation is *not*

increased, so downward velocity is *increased* at depths more than 0.5 m into the mold cavity.

4. Increasing SEN depth with EMBr (0.355 T) has almost exactly the *opposite* effects as increasing EMBr listed above. This is because the jet tends to move below the EMBr region, so is less affected by the EMBr field. The only exceptions are that in both cases, the upper recirculation zone is expanded and jet penetration into the lower recirculation zone is deepened.

ACKNOWLEDGMENTS

The authors thank Ron O'Malley and Nucor Steel (Decatur, AL) for their assistance and use of their facilities for the experimental portion of this work. They also thank the Continuous Casting Consortium, University of Illinois at Urbana–Champaign, and the National Science Foundation (Grant No. DMI 05-00453) for support of this project.

REFERENCES

1. *World Steel in Figures*, International Iron and Steel Institute, Brussels, Belgium, 2006, www.worldsteel.org.
2. M.M. Wolf: *Steelmaking Conf. Proc.*, Toronto, 1992, ISS, Warrendale, PA, 1992, pp. 83–137.
3. J. Herbertson: *74th Steelmaking Proc. of Iron & Steel Society*, Washington, DC, 1991.
4. K. Okazawa, T. Takehito, J. Fukuda, T. Kawase, and M. Toki: *ISIJ Int.*, 2001, vol. 41 (8), pp. 851–58.
5. H.R. Hackl, A.F. Lehman, J.E.A. Eriksson, and S.G. Kollberg: *AISTech Preliminary Program*, AIST, Warrendale, PA, 2006.
6. J. Nakashima, J.A. Kiyose, Y. Ohtani, J. Fukuda, T. Kawase, and M. Doki: Nippon Steel Technical Report No. 86, Nippon Steel, 2002, No. 86, pp. 61–67.
7. T. Ishii, S.S. Sazhin, and M. Makhlouf: *Iron Steelmaking*, 1996, vol. 23 (3), pp. 267–72.
8. J. Kubota, K. Okimoto, A. Shirayama, and H. Murakami: *74th Steelmaking Conf. Proc.*, ISS-AIME, Warrendale, PA, 1991, pp. 233–38.
9. P.H. Dauby and S. Kunstreich: *Ironmaking and Steelmaking*, 2005, vol. 32 (1), pp. 80–86.
10. P.M. Lofgren and P. Hanley: *AISTech Conf. Proc.*, 2004, vol. 2, pp. 977–84.
11. M.Y. Ha, H.G. Lee, and S.H. Seong: *J. Mater. Process. Technol.*, 2003, vol. 133 (3), pp. 322–39.
12. K. Takatani, K. Nakai, N. Kasai, T. Watanabe, and H. Nakajima: *ISIJ Int.*, 1989, vol. 29 (12), pp. 1063–68.
13. D.S. Kim, W.S. Kim, and K.H. Cho: *ISIJ Int.*, 2000, vol. 40 (7), pp. 670–76.
14. H. Harada, T. Toh, T. Ishii, K. Kaneko, and E. Takeuchi: *ISIJ Int.*, 2001, vol. 41 (10), pp. 1236–44.
15. M. Zeze, H. Harada, E. Takeuchi, and T. Ishii: *76th Steelmaking Conf.*, Dallas, TX, Mar. 1993, pp. 267–72.
16. A. Idogawa, M. Sugizawa, S. Takeuchi, K. Sorimachi, and T. Fujii: *Mater. Sci. Eng. A*, 1993, vol. A173 (1–2), pp. 293–97.
17. B. Li, T. Okane, and T. Umeda: *Metall. Trans. B*, 2000, vol. 31B, pp. 1491–1503.
18. B.G. Thomas, Q. Yuan, S. Sivaramakrishnan, T. Shi, S.P. Vanka, and M.B. Assar: *ISIJ Int.*, 2001, vol. 41 (10), pp. 1266–76.
19. Q. Yuan, B. Zhao, S.P. Vanka, and B.G. Thomas: *Steel Res. Int.*, 2005, vol. 76 (1,Special Issue: Simulation of Fluid Flow in Metallurgy), pp. 33–43.
20. Q. Yuan, S. Sivaramakrishnan, S.P. Vanka, and B.G. Thomas: *Metall. Mater. Trans. B*, 2004, vol. 35B, pp. 967–82.
21. B.E. Launder and D.B. Spalding: *Mathematical Models of Turbulence*, Academic Press, London, 1972, pp. 90–111.
22. *FLUENT6.2-Manual*, Fluent, Inc., Lebanon, NH, 2005.
23. D.E. Hershey, B.G. Thomas, and F.M. Najjar: *Int. J. Numer. Methods Fluids*, 1993, vol. 17 (1), pp. 23–47.
24. Y. Meng and B.G. Thomas: *Metall. Mater. Trans. B*, 2003, vol. 34B, pp. 685–705.
25. B.T. Rietow: Master's Thesis, University of Illinois at Urbana–Champaign, Urbana, IL, 2007.
26. H. Bai and B.G. Thomas: *Metall. Mater. Trans. B*, 2001, vol. 32B, pp. 253–67.
27. *Integrity Design and Research Corporation*, http://www.gaussmeter.info/dc-gauss.html.
28. R. McDavid and B.G. Thomas: *Metall. Trans. B*, 1996, vol. 27B, pp. 672–85.
29. E. Takeuchi and J.K. Brimacombe: *Metall. Trans. B*, 1984, vol. 15B, pp. 493–509.
30. R. Moreau: *Magnetohydrodynamics*, Kluwer Academic Pub. Co, Norwell, MA, 1990, pp. 110–64.
31. M.J. Cho, I.C. Kim, S.J. Kim, and J.K. Kim: *Trans. KSME*, 1999, vol. 23B (13), pp. 1491–1502.
32. K. Rackers and B.G. Thomas: *78th Steelmaking Conf. Proc.*, Nashville, TN, Apr. 2, 1995, ISS, Warrendale, PA, vol. 78, pp. 723–34.
33. D.T. Creech: Master's Thesis, University of Illinois at Urbana–Champaign, Urbana, IL, 1999.